



Faculty of Liberal Arts & Sciences

2023

A Tale of Three Dwarfs: No Extreme Cluster Formation in Extreme Star-forming Galaxies

Chandar, Rupali, Caputo, Miranda, Mok, Angus, Linden, Sean, Whitmore, Bradley C., Toscano, Aimee, Conyer, Jaidyn, Cook, David O., Lee, Janice C., Ubeda, Leonardo and White, Richard

Suggested citation:

Chandar, Rupali, Caputo, Miranda, Mok, Angus, Linden, Sean, Whitmore, Bradley C., Toscano, Aimee, Conyer, Jaidyn, Cook, David O., Lee, Janice C., Ubeda, Leonardo and White, Richard (2023) A Tale of Three Dwarfs: No Extreme Cluster Formation in Extreme Star-forming Galaxies. *The Astrophysical Journal*, 949 (2). p. 116. ISSN 0004-637X
Available at <https://openresearch.ocadu.ca/id/eprint/4147/>

Open Research is a publicly accessible, curated repository for the preservation and dissemination of scholarly and creative output of the OCAD University community. Material in Open Research is open access and made available via the consent of the author and/or rights holder on a non-exclusive basis.

The OCAD University Library is committed to accessibility as outlined in the [Ontario Human Rights Code](#) and the [Accessibility for Ontarians with Disabilities Act \(AODA\)](#) and is working to improve accessibility of the Open Research Repository collection. If you require an accessible version of a repository item contact us at repository@ocadu.ca.



A Tale of Three Dwarfs: No Extreme Cluster Formation in Extreme Star-forming Galaxies

Rupali Chandar¹ , Miranda Caputo¹ , Angus Mok² , Sean Linden³ , Bradley C. Whitmore⁴ , Aimee Toscano⁵,
Jaidyn Conyer⁶, David O. Cook⁷ , Janice C. Lee⁸ , Leonardo Ubeda⁴, and Richard White⁴

¹ Ritter Astrophysical Research Center, University of Toledo, Toledo, OH 43606, USA; rupali.chandar@utoledo.edu

² OCAD University, Toronto, Ontario, M5T 1W1, Canada

³ Department of Astronomy, University of Massachusetts at Amherst, Amherst, MA 01003, USA

⁴ Space Telescope Science Institute, 3700 San Martin Drive, Baltimore, MD 21218, USA

⁵ Washington and Jefferson College, Washington, PA 15301, USA

⁶ University of Akron, Akron, OH 44304, USA

⁷ Caltech/IPAC, 1200 E. California Boulevard, Pasadena, CA 91125, USA

⁸ Gemini Observatory/NSFs NOIRLab, 950 N. Cherry Avenue, Tucson, AZ 85719, USA

Received 2022 November 22; revised 2023 March 28; accepted 2023 March 29; published 2023 June 5

Abstract

Nearly all current simulations predict that outcomes of the star formation process, such as the fraction of stars that form in bound clusters (Γ), depend on the intensity of star formation activity (Σ_{SFR}) in the host galaxy. The exact shape and strength of the predicted correlations, however, vary from simulation to simulation. Observational results also remain unclear at this time, because most works have mixed estimates made from very young clusters for galaxies with higher Σ_{SFR} with those from older clusters for galaxies with lower Σ_{SFR} . The three blue compact dwarf (BCD) galaxies ESO 185-IG13, ESO 338-IG04, and Haro 11 have played a central role on the observational side because they have some of the highest known Σ_{SFR} and published values of Γ . We present new estimates of Γ for these BCDs in three age intervals (1–10 Myr, 10–100 Myr, 100–400 Myr), based on age-dating, which includes H α photometry to better discriminate between clusters younger and older than ≈ 10 Myr. We find significantly lower values for Γ (1–10 Myr) than published previously. The likely reason for the discrepancy is that previous estimates appear to be based on age–reddening results that underestimated ages and overestimated reddening for many clusters, artificially boosting Γ (1–10 Myr). We also find that fewer stars remain in clusters over time, with $\approx 15\%$ – 39% in 1–10 Myr clusters, $\approx 5\%$ – 7% in 10–100 Myr clusters, and $\approx 1\%$ – 2% in 100–400 Myr clusters. We find no evidence that Γ increases with Σ_{SFR} . These results imply that cluster formation efficiency does not vary with star formation intensity in the host galaxy. If confirmed, our results will help guide future assumptions in galaxy-scale simulations of cluster formation and evolution.

Unified Astronomy Thesaurus concepts: [Blue compact dwarf galaxies \(165\)](#); [Star clusters \(1567\)](#); [Young massive clusters \(2049\)](#)

1. Introduction

Stars and clusters form in the densest regions of molecular clouds (e.g., Lada & Lada 2003; McKee & Ostriker 2007). Star clusters are therefore intricately tied to the star formation process. One key goal is to understand how conditions in the star-forming interstellar medium imprint onto young star and cluster populations. These are typically characterized by two fundamental parameters, the star and cluster formation efficiencies. The latter quantity, which is the fraction of stars that form in gravitationally bound clusters, known as Γ , has played a prominent role in theoretical and observational studies over the past decade.

The most striking theoretical claim about Γ is that it increases systematically with the intensity of star formation, which can be traced using the star formation rate (SFR) per unit area or Σ_{SFR} . Early analytic frameworks relied on scaling relations to map cluster formation efficiency to the density spectrum of the interstellar medium and to Σ_{SFR} (Krujissen 2012). In the intervening decade, new galaxy-scale

simulations have used a variety of approaches (including MHD, N -body, semianalytic) and physical scales to predict the relationship between star and cluster formation. The simulations account for different subsets of the relevant physics either self-consistently or with sub-resolution models to track the formation (and evolution) of entire cluster populations in dwarf-mass (e.g., Lahén et al. 2019) and Milky Way-mass (e.g., Grudić et al. 2022) galaxies. While they rely on a number of assumptions and prescriptions for (unresolved) star formation and stellar feedback, nearly all find that Γ increases with Σ_{SFR} (e.g., Krujissen 2012; Li et al. 2017, 2018; Grudić et al. 2018, 2022; Lahén et al. 2019; Pfeffer et al. 2019).

As shown in Figure 1, the exact dependence of Γ on Σ_{SFR} varies between simulations. The early Krujissen (2012) work predicted a ~ 100 -fold increase in Γ , from less than 1% at low Σ_{SFR} ($\lesssim 0.001 M_{\odot} \text{ yr}^{-1} \text{ kpc}^{-2}$) to approaching 100% at high Σ_{SFR} ($\gtrsim 1 M_{\odot} \text{ yr}^{-1} \text{ kpc}^{-2}$). A mapping of the giant molecular clouds in a FIRE-2 simulation onto a model cluster population predicts a more modest increase in Γ by a factor of ≈ 10 over the same Σ_{SFR} range (Grudić et al. 2022), while other works predict shallower increases of factors ~ 2.5 – 4 , depending on the specific star formation and feedback parameters that are adopted (Li et al. 2018). Recently, Dinnbier et al. (2022) pointed out that changes in the assumptions (for, e.g., the exact treatment of a star formation threshold and stellar feedback

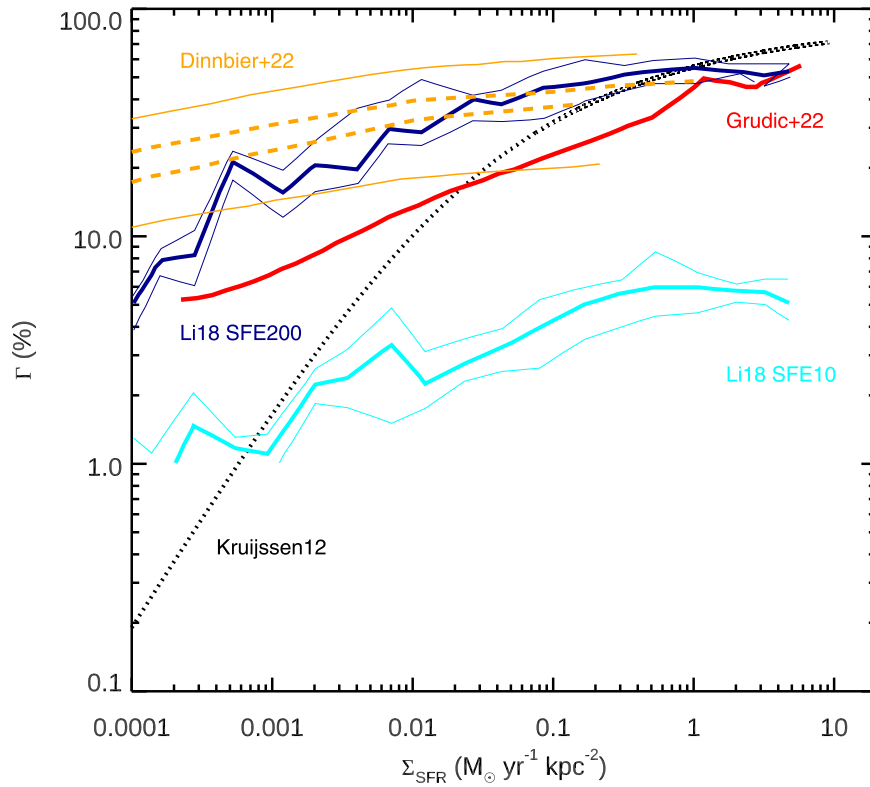


Figure 1. Predictions of the fraction of stars that form in bound clusters Γ vs. Σ_{SFR} , from five different simulations of cluster formation. The predictions are reproduced from Kruijssen (2012), Li et al. (2018), Dinnbier et al. (2022), and Grudić et al. (2022), as indicated. The main point is that the current generation of simulations predict an increase in cluster formation efficiency Γ between a factor of ≈ 100 (Kruijssen 2012) at the upper end and 1.5 (Dinnbier et al. 2022) at the lower end, over the range 0.001 to $1 M_{\odot} \text{ yr}^{-1} \text{ kpc}^{-2}$ in Σ_{SFR} .

processes among others) can have a large impact on the predictions for Γ ; they find a weak dependence (factor of ~ 1.5) of Γ on Σ_{SFR} in their preferred model, shown in orange in Figure 1.

The observational picture is also unclear. While many works have claimed that Γ increases with Σ_{SFR} (e.g., Goddard et al. 2010; Cook et al. 2012; Adamo et al. 2015, 2020; Johnson et al. 2016; Ginsburg & Kruijssen 2018), this trend arises, at least in part, because these works have compared estimates for Γ calculated from different age intervals in different galaxies. At the low- Σ_{SFR} end ($\approx 0.001 M_{\odot} \text{ yr}^{-1} \text{ kpc}^{-2}$), estimates have mostly been made from 10 to 100 Myr clusters. Key examples are $\Gamma_{10-100 \text{ Myr}} \sim 5.8\%$ and $\sim 4.2\%$ for the LMC and SMC, respectively (Goddard et al. 2010), and $\sim 4\%$ – 8% for M31 (Johnson et al. 2016). At the high- Σ_{SFR} end ($\approx 1 M_{\odot} \text{ yr}^{-1} \text{ kpc}^{-2}$), estimates rely on 1–10 Myr clusters. This includes results for the blue compact dwarf (BCD) galaxies that are the subject of this work, with published values of $\Gamma_{1-10 \text{ Myr}} \sim 50\%$ for ESO 338 and Haro 11 (Adamo et al. 2011b) and 26% for ESO 185 (Adamo et al. 2010). It also includes the more massive, luminous infrared galaxies observed as part of the HiPeec survey (NGC 34, NGC 1614, NGC 3256, NGC 3690, NGC 4194, and NGC 6052), but which show no trend in $\Gamma_{1-10 \text{ Myr}}$ over a factor of ≈ 10 in Σ_{SFR} (see their Figure 18; Adamo et al. 2020). Because clusters naturally dissolve over time, mixing results from different age intervals can artificially imprint the claimed correlation (Chandar et al. 2017).

At least some of the confusion in the observational literature has likely been driven by the desire to include only bound clusters. However, it is not possible to assess whether clusters

are bound (have negative total energy) or unbound, based on currently available information. This means that extragalactic cluster catalogs include an unknown fraction of bound and unbound clusters at ages younger than $\lesssim 10$ Myr. After this time, most remaining clusters are likely bound, although their observed age distributions suggest that they continue to lose mass and dissolve more or less continuously (e.g., Fall et al. 2005; Chandar et al. 2010a; Whitmore et al. 2010; Fall & Chandar 2012). With these competing considerations in mind, we will perform the same calculations to estimate the fraction of stars found in clusters in three age intervals, 1–10 Myr, 10–100 Myr, and 100–400 Myr, and refer to the results as $\Gamma_{1-10 \text{ Myr}}$, $\Gamma_{10-100 \text{ Myr}}$, and $\Gamma_{100-400 \text{ Myr}}$, respectively.

In this work we revisit estimates of the cluster formation efficiency for the BCD galaxies ESO 185-IG13, ESO 338-IG04, and Haro 11, which have new WFC3 observations with the Hubble Space Telescope (HST) taken as part of the “Clusters, Clumps, Gas, and Dust (CCDG) in Extreme Star-forming Galaxies” project (GO-15649, PI: Chandar). Together with the luminous infrared HiPeec galaxies (which we will study in a future work), these BCDs hold up the high end of Σ_{SFR} . The rest of this paper is organized as follows. In Section 2, we summarize basic properties of our BCD sample, and present new cluster catalogs, including important updates on cluster age-dating. At the end of this section we make a number of checks of cluster ages and identify some weaknesses in previous age-dating of these galaxies. The cluster mass functions are presented in Section 3, along with the results of maximum likelihood fits of the Schechter function to assess the shape at the high-mass end. In Section 4 we calculate the fraction of stars found in clusters, compare our results with

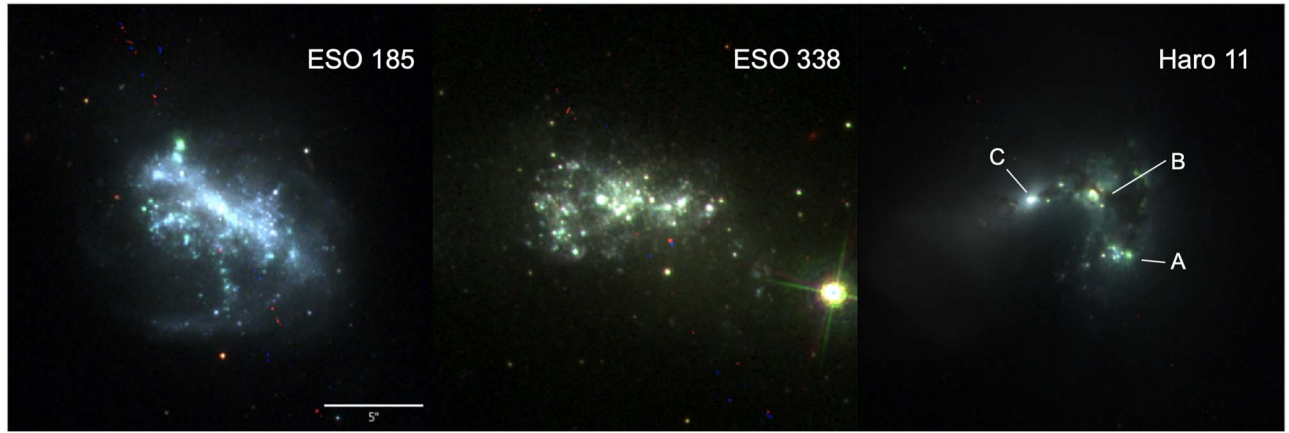


Figure 2. Three-color $B-V-I$ images of the blue compact dwarf galaxies taken with the Hubble Space Telescope show hundreds of clusters with a broad range of colors (and hence ages). Green point sources are $H\alpha$ emitters in ESO 185-IG13 (left) and Haro 11 (right). The scale bar is $5''$ long.

Table 1
Dwarf Galaxy Sample

Galaxy Name	Distance (Mpc)	Foreground $E(B-V)$ (mag)	SFR ^a ($M_{\odot} \text{ yr}^{-1}$)	Area (kpc^2)	Σ_{SFR} ($M_{\odot} \text{ yr}^{-1} \text{ kpc}^{-2}$)
ESO 185-IG13	76	0.048	4.6	12.3	0.38
ESO 338-IG04	38	0.076	2.3	2.0	1.15
Haro 11	82	0.010	17.4	10.2	1.7

Note

^a The star formation rates have been converted from an assumed Salpeter IMF to a Chabrier IMF by dividing by 1.38.

those available for galaxies at the low- Σ_{SFR} end, and discuss the implications. Our main results and conclusions are summarized in Section 5. We also include an Appendix, which presents the shape of the cluster mass functions (a step along the way to calculating Γ) in these BCDs for the first time, and perform a maximum likelihood fit to a Schechter function.

2. Galaxy Sample and Cluster Catalogs

2.1. Galaxy Properties

Color images of ESO 185, ESO 338, and Haro 11 taken in the $B-V-I$ filters with the HST are shown in Figure 2. ESO 185 has a bright, bar-like structure crossing the center, and tidal features indicating the system experienced a recent merging event. Recent star and cluster formation is more evenly spread throughout ESO 338 than in ESO 185. BCDs in general have low internal extinction (e.g., Mas-Hesse & Kunth 1999). Haro 11, which has three bright “knots” (labeled A, B, C), is the only one of the three galaxies to show limited dusty regions. We adopt the same distances as Adamo et al. (2010, 2011a) to each galaxy, and compile this information in Table 1.

We adopt $H\alpha$ -based estimates of the star formation rate, since this tracer is sensitive to only the most recent (≈ 10 Myr) star formation (e.g., Kennicutt & Evans 2012), and a close match to the 1–10 Myr interval used to determine Γ . Adamo et al. (2010, 2011a) and Hayes et al. (2007, Haro 11) used the Kennicutt (1998) calibration to convert total $H\alpha$ luminosity to SFR for each galaxy. However, this calibration assumes a Salpeter stellar initial mass function (IMF), whereas we adopt a Chabrier (2003) IMF when we estimate cluster masses in

Section 2.4.⁹ We therefore divide the published $H\alpha$ -based SFRs by a factor of 1.38 to account for the difference between the Salpeter and Chabrier IMFs. The corrected SFRs are $4.6 M_{\odot} \text{ yr}^{-1}$ (ESO 185), $2.3 M_{\odot} \text{ yr}^{-1}$ (ESO 338), and $17.4 M_{\odot} \text{ yr}^{-1}$ (Haro 11), and are compiled in column 4 of Table 1.

In BCDs, star formation is confined to an area that is ≈ 100 times smaller than a typical spiral disk. We adopt the same area (in kpc^2) as Adamo et al. (2010, 2011a) (listed in column 5 of Table 1). The moderate-to-high rates of star formation contained within a small area lead to very high values of Σ_{SFR} : 0.38 (ESO 185), 1.15 (ESO 338), and $1.7 M_{\odot} \text{ yr}^{-1} \text{ kpc}^{-2}$ (Haro 11), compared with $\sim 0.01 M_{\odot} \text{ yr}^{-1} \text{ kpc}^{-2}$ for spiral galaxies like M51 and M83 (e.g., Adamo et al. 2015; Chandar et al. 2017). Dwarf irregular galaxies like the LMC and SMC have Σ_{SFR} that are lower than Σ_{SFR} in spirals by a factor of ≈ 10 (e.g., Goddard et al. 2010; Cook et al. 2019; Whitmore et al. 2020), and hence lower than in the BCDs studied here by a factor of ≈ 1000 .

There are several inherent sources of uncertainty in the SFR estimates, including measurements of flux, variations in the SFR, the lower metallicity of our galaxies, and the leakage of Lyman continuum photons from the parent galaxy.¹⁰ Following Cook et al. (2023), we adopt a 25% uncertainty in the SFR estimates.

⁹ Adamo et al. (2010, 2011a) adopted a Kroupa IMF (similar to the Chabrier IMF assumed here) when estimating cluster masses, but used $H\alpha$ -based star formation rates that assumed a Salpeter IMF.

¹⁰ Haro 11 is, in fact, well known to leak these ultraviolet photons.

Table 2
WFC3 Filters and Exposure Times

Galaxy	NUV (F275W)	<i>U</i> (F336W)	<i>B</i> (F438W)	<i>V</i> (F555W)	<i>I</i> (F814W)	H α (F665N)	Pa β (F130N)	H (F160W)
ESO 185-IG13	1935	...	1890	2680	1800	1905	800	1600
ESO 338-IG04	1965	...	1500	830	1350	...	1802	2400
Haro 11	1920	1332	680	1740	1740	1800	800	1600

2.2. Data, Detection, and Photometry

HST has imaged ESO 185, ESO 338, and Haro 11 in broadband and narrowband filters covering the near-ultraviolet (NUV) to the near-infrared. The observations used in this work are a mix of new and archival images, with the new data taken as part of our CCDG program (GO-15649; PI: Chandar) with the WFC3 camera (see Table 2). We primarily use observations in the NUV (F275W), *U* (F336W), *B* (ACS/F435W or WFC3/F438W), *V* (WFC3/F555W or ACS/F550M), H α (F658N), and *I* (F814W) filters, but we checked for highly reddened sources in Haro 11 using the Pa β (F130N) and H (F160W) images as well. The lower resolution of the near-infrared images makes photometry in these bands less useful for age-dating. ESO 185 and ESO 338 have not been imaged in the *U* band, and ESO 338 also does not have H α imaging.

Individual exposures are processed through the standard Pyraf/STSDAS CALACS or CALWFC3 software, then aligned and drizzled onto a common grid to create one image for each filter using the DRIZZLEPAC software package. The *V*-band image is used as the reference in each case, with a pixel scale of 0.''04 (the native WFC3 pixel scale), and astrometry calibrated with Gaia DR2 sources (Gaia Collaboration et al. 2018). Sky subtraction is performed during the drizzling process and the output images are all oriented with north up and east to the left. The final FITS files are in units of electrons per second.

At the distances of the three BCDs in our sample, stellar clusters appear essentially as point sources. We run the DAOFIND detection algorithm on the *V*-band image in each galaxy with a 3σ detection limit. Aperture photometry was performed in a two-pixel radius for all sources in all broadband filters, with an annulus with radii between 7 and 9 pixels to determine the background level. These apertures were selected because they minimize the scatter in the measured colors of clusters compared with predictions from stellar evolutionary models. We convert the apparent magnitudes to the VEGAMag system by applying the following zero-points: 22.640 (WFC3/F275W), 23.526 (WFC3/F336W), 25.764 (ACS/F438W), 25.832 (WFC3/F555W), and 25.518 (WFC3/F814W). Filter-dependent aperture corrections were determined from isolated sources and applied to obtain the total apparent magnitude for each cluster. Photometric errors include uncertainties in both source counts and background levels.

The narrowband H α images, which trace warm ionized gas, sometimes have a very different morphology than the stellar emission that dominates the broadband images. Feedback from recently formed massive cluster stars quickly pushes the surrounding ionized gas into bubbles and partial shells with a range of radii. We therefore do not include background subtraction in the aperture photometry performed on the non-continuum-subtracted narrowband images.

We select clusters to have a measured *V*-band magnitude brighter than 27.0 mag, and to have a concentration index between 1.0 and 2.4 (concentration index is the difference in

aperture magnitudes in the *V* band determined using radii of 2 pixels and 0.5 pixels). The upper limit selected for the measured concentration index eliminated detections of diffuse regions within the galaxies, while the lower limit eliminated a handful of cosmic-ray residuals. The main sources of contamination that remain after these selection criteria are foreground stars and background galaxies. We performed a final visual inspection of the detected sources in all three galaxies to remove remaining contaminants. Figure 3 shows clusters detected in a crowded star-forming region and an outer region of Haro 11. ESO 185 and Haro 11 each contain objects that appear to be nuclei or nuclear clusters (a single object at the dynamical center of ESO 185, and three very bright point sources in Haro 11). We do not include these sources as part of the cluster analysis. The final cluster catalogs contain 213/596 (ESO 185), 300/399 (ESO 338), and 180/536 (Haro 11) candidate clusters brighter than $m_V = 24.5/27.0$; clusters with m_V of 24.5 mag and brighter have a median uncertainty of ≈ 0.2 mag in the NUV filter.

2.3. Color–Color Diagrams and Constraints on Reddening

The NUV – *B* versus *V* – *I* color–color diagrams of the cluster populations in the three dwarf galaxies are shown in Figure 4. All detected clusters in ESO 185 (left panel), ESO 338 (middle panel), and Haro 11 (right panel) are shown as gray circles, and clusters brighter than m_V of 24.5 mag are shown as black circles. The cluster colors have been corrected for the foreground reddening values given in Table 1. The arrow in the right panel shows the direction in which additional reddening would move a cluster, assuming a Milky Way-type extinction law (Fitzpatrick 1999). Each panel also shows predictions from the Bruzual & Charlot (2003) stellar population models¹¹ for $1/5 \times$ solar (blue solid line) and solar metallicity (red dashed line). The models predict the color (and luminosity) evolution of clusters starting soon after their birth at 1 Myr (upper left), through the ages of globular clusters around ~ 12 Gyr in the lower right, and do not include any contribution from nebular line emission.

We see that, in aggregate, the cluster colors, especially the black points brighter than m_V of 24.5 mag, closely follow the predicted model tracks, except for a handful of sources in Haro 11 that are to the right of the BC03 models. This suggests that the overall cluster populations in these BCDs do not experience much reddening due to dust. After examining colors in different locations, we find that only clusters in the region around and to the west of Knot B in Haro 11 have any appreciable reddening. We perform age-dating experiments, which show that a maximum $E(B - V) \approx 0.5$ mag ($A_V \approx 1.5$ mag) (when H α photometry is included in the spectral energy

¹¹ We previously tested several different models, and found that, overall, the Bruzual & Charlot (2003, hereafter BC03) population synthesis models best match the observed colors of young star clusters (e.g., Chandar et al. 2010b; Turner et al. 2021).

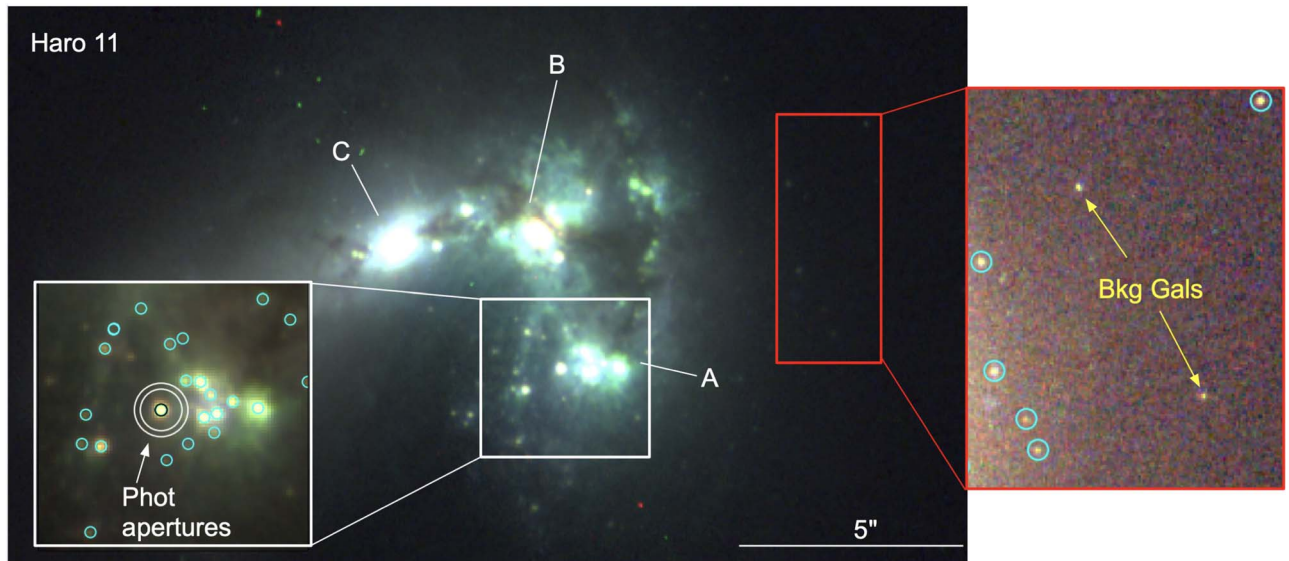


Figure 3. Three-color $B-V-I$ image and zoom-in to a crowded, actively star-forming region dominated by young, $\sim 15\text{--}20$ Myr clusters (outlined in white), and another region toward the outskirts dominated by clusters older than 100 Myr (outlined in red). In the star-forming region we only show the locations of clusters brighter than 23.5 mag in the V band, since it is hard to show bright and faint clusters in the same stretch. The 2 pixel aperture used to perform photometry, and the 7 and 9 pixel annuli used for background subtraction are also shown. Two background galaxies that were excluded from our cluster catalog are identified in the outer region.

distribution (SED fitting) is sufficient to successfully age-date the handful of reddened young clusters in this area.

We also produced CO(1–0) moment-0 emission line maps of Haro 11 from archival data taken by the Atacama Large Millimeter/submillimeter Array (ALMA; 2013.1.00350.S). These contours are shown in Figure 5 superposed on a color HST image. The strongest peaks of CO emission are coincident with a bright optical region, not with the dustiest parts of the galaxy where a handful of reddened young clusters are found (although we do find lower levels of CO emission from these dusty regions). We also see little CO in the region toward the south (Knot A), which has recently formed many of the most massive clusters. No Pa β -emitting sources are revealed in this dusty area, indicating that either clusters are not currently forming in these regions, or if they are they remain deeply buried, with $A_V \gtrsim 7\text{--}10$ mag.

3. Cluster Age-dating

3.1. Method and Checks

To estimate the mass, age, and reddening of each cluster in the three BCD galaxies, we follow the general SED fitting technique described in Chandar et al. (2010b), but with an updated treatment of the reddening. We estimate the age (τ) and extinction (A_V) for each cluster by performing a least χ^2 fit comparing the observed cluster magnitudes with predictions from the $1/5 \times$ solar BC03 population model. The grid runs over ages from $\log(\tau/\text{yr}) = 6.0$ to 10.2, and from $E(B-V) = 0.0$ mag up to a maximum value. Most works adopt a single maximum $E(B-V)$ value for the entire cluster population during SED fitting, based on the idea that sightlines to some individual clusters may be highly reddened. For example, a maximum $E(B-V)$ of 1.5 mag was adopted by the LEGUS (Calzetti et al. 2015) and PHANGS (e.g., Turner et al. 2021; Lee et al. 2022) cluster surveys, and by Adamo et al. (2010, 2011a) for the clusters in ESO 185-IG13, ESO 338-IG04, and Haro 11. However, adopting a single, large value

like 1.5 mag for the maximum $E(B-V)$ can result in serious problems in the estimated ages for clusters older than ≈ 10 Myr, as explored and discussed in detail by Whitmore et al. (2020, 2023).

Here, we use a more direct approach and allow the adopted maximum $E(B-V)$ value used during SED fitting to vary based on observations and inferences about the clusters themselves. As noted earlier, color-color diagram of clusters in ESO 185 and ESO 338 (Figure 4) show very little reddening toward nearly the entire cluster population. We therefore adopt a maximum $E(B-V) = 0.1$ mag for all clusters in these two galaxies during SED fitting, but also check the impact of adopting maximum values of 0.5 mag and 1.0 mag in the age-dating. While most clusters in Haro 11 also follow the BC03 models, there are a handful in the dusty region near Knot B that fall off the BC03 model tracks along the reddening vector. These clusters have H α emission, and therefore are $\approx 3\text{--}6$ Myr old. If we compare their observed colors with those predicted for these young ages, these clusters should have $E(B-V) \approx 0.5$ mag. For Haro 11, we therefore adopt a maximum reddening of $E(B-V) = 0.5$ mag for the reddened clusters near Knot B, and $E(B-V) = 0.1$ mag for the rest.

The best-fit values of τ and A_V minimize the statistic $\chi^2(\tau, A_V) = \sum_{\lambda} W_{\lambda} (m_{\lambda}^{\text{obs}} - m_{\lambda}^{\text{mod}})^2$ where m_{λ}^{obs} and m_{λ}^{mod} are the observed and model magnitudes respectively, and the sum runs over all available broadband and narrowband filters NUV, U , B , V , H α , and I . The weight factors in the formula χ^2 are taken to be $W_{\lambda} = (\sigma_{\lambda}^2 + 0.05^2)^{-1}$, where σ is the photometric uncertainty. The mass of each cluster is estimated from the observed V -band luminosity, corrected for extinction, and the (present-day) age-dependent mass-to-light ratios (M/L_V) predicted by the models, assuming the distances compiled in Table 1. We note that correcting for reddening internal to a cluster can significantly boost its estimated mass in some cases. For example, a reddening of $E(B-V) \approx 0.5$ mag corresponds to $A_V \approx 1.6$ mag, which would boost the intrinsic luminosity

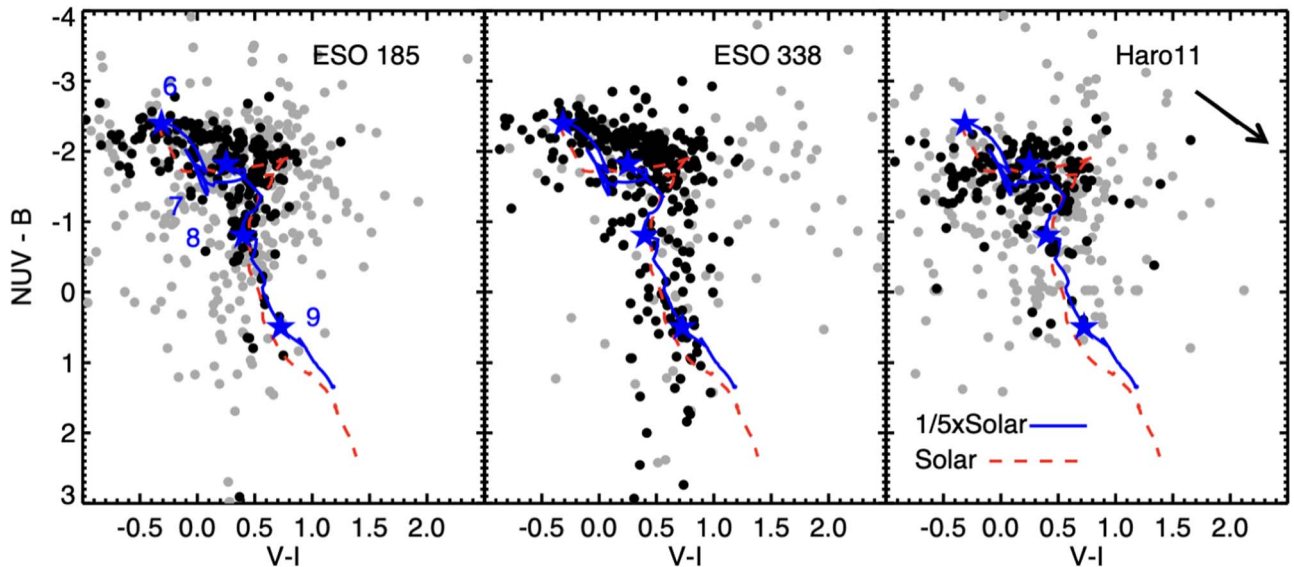


Figure 4. $NUV - B$ vs. $V - I$ color-color diagrams for clusters detected in our blue compact dwarf galaxies. The solid lines in each panel show the $1/5 \times$ solar metallicity predictions from the BC03 models appropriate for these dwarf galaxies. The dashed lines show predictions from the solar metallicity BC03 model. The arrow in the right panel shows the direction in which reddening will move cluster colors. All clusters with photometry in the NUV, B , V , and I bands are shown as gray points, and clusters brighter than $m_V \approx 24.5$ mag are shown as black points. The main point is that the measured cluster colors follow the model predictions quite well, indicating that, overall, reddening does not significantly affect cluster colors.

and hence cluster mass by a factor of more than 4 for a given age and mass-to-light ratio.

The largest source of uncertainty in the age estimates comes from uncertainties in the photometry, particularly in the NUV and U -band measurements for the fainter clusters. Our method typically produces uncertainties at the level of $\log(\tau/\text{yr}) \approx 0.3$ (factor of ≈ 2); see, e.g., Chandar et al. (2010b). The uncertainties in the mass estimates are tied to those in the ages and to a lesser degree to the best-fit reddening. The clusters in our study are sufficiently massive that stochastic fluctuations should not have much impact on their colors.

Our method, which allows for a flexible maximum A_V in the SED fitting based on the amount of reddening in a given region, improves age results for clusters in Haro 11. Specifically, the bright cluster located at R.A. = 00:36:52.41 and decl. = $-33:33:16.58$ in Knot B (see Figure 5) has red broadband colors, but some $H\alpha$ emission right on top of and next to it. Our age-dating method (which includes $H\alpha$ for Haro 11) finds $\log(\tau/\text{yr}) \approx 9$ when a maximum $E(B - V)$ of 0.1 mag is imposed, but $\log(\tau/\text{yr}) \approx 6.98$ when a maximum $E(B - V)$ of 0.5 mag is assumed instead. The final cluster age-mass results are shown in Figure 6.

We perform a number of checks of our age-dating results. One important takeaway is that our method returns estimated ages younger than 10 Myr for clusters with obvious $H\alpha$ emission regardless of whether we adopt a maximum $E(B - V)$ of 0.1, 0.5, or 1.0 mag in the SED fitting; the handful of highly reddened, very young clusters in Haro 11 discussed in Section 3.1 are the only exceptions, and require $E(B - V)$ of at least 0.5 mag. Adopting a maximum $E(B - V)$ of 0.5 or 1.0 mag affects only $\approx 7\%$ of the sample, predominantly clusters fainter than $m_V \sim 25$ mag, and systematically changes their estimated ages from ~ 30 to 500 Myr with little reddening to just under 10 Myr with moderate reddening. It is hard to draw firm conclusions about the actual ages of these faint clusters, although most of them are in regions with little dust, suggesting they are likely faded, older clusters.

We visually inspected every cluster with $M \geq 10^5 M_\odot$ in color images. In Figure 6 we include postage stamp images of four massive clusters in each galaxy as illustrative examples. In each case, clusters designated “1” highlight one cluster younger than 10 Myr, which is typically the brightest $H\alpha$ -emitting source in its parent galaxy. Clusters designated “2” all have best-fit ages between ~ 15 and 30 Myr, with blue colors but no associated $H\alpha$ emission. Clusters designated “3” and “4” are somewhat older, with redder colors (but no associated dust) and no $H\alpha$ emission.

As mentioned earlier, Haro 11 is the only BCD in our sample that has appreciable dust. Our results indicate that some massive clusters in Haro 11 have ages ≈ 3 –6 Myr (e.g., cluster “1” in the right panel of Figure 6), while other massive clusters have ages ≈ 15 –20 Myr (e.g., cluster “2”). One potential concern is that the clusters assigned ages of ≈ 15 –20 Myr are actually younger, but moderately reddened. An inspection of all clusters more massive than $10^5 M_\odot$ confirms that those with estimated ages of ≈ 15 –20 Myr have no associated $H\alpha$ emission or visible dust, as seen in the postage stamps included in Figure 5. Therefore the age-dating method appears to be able to correctly differentiate between and age-date clusters formed ≈ 3 –6 Myr ago from those formed ≈ 15 –20 Myr ago.

3.2. Comparison with Previous Works

The cluster populations of ESO 185, ESO 338, and Haro 11 were previously studied by Adamo et al. (2010, 2011b) based on earlier HST imaging, some with the WFPC2 camera. While we do not have access to their catalogs, we are able to make some global comparisons. Our cluster catalogs have at least twice as many clusters as the earlier ones, likely driven by the shallower observations in the three bluest filters that were available to Adamo and collaborators more than a decade ago. They presented mass-age and reddening-age diagrams for clusters in ESO 185 and Haro 11, allowing us to make some comparisons of age-dating results for these two galaxies. The ages and masses of clusters in Haro 11 were more recently

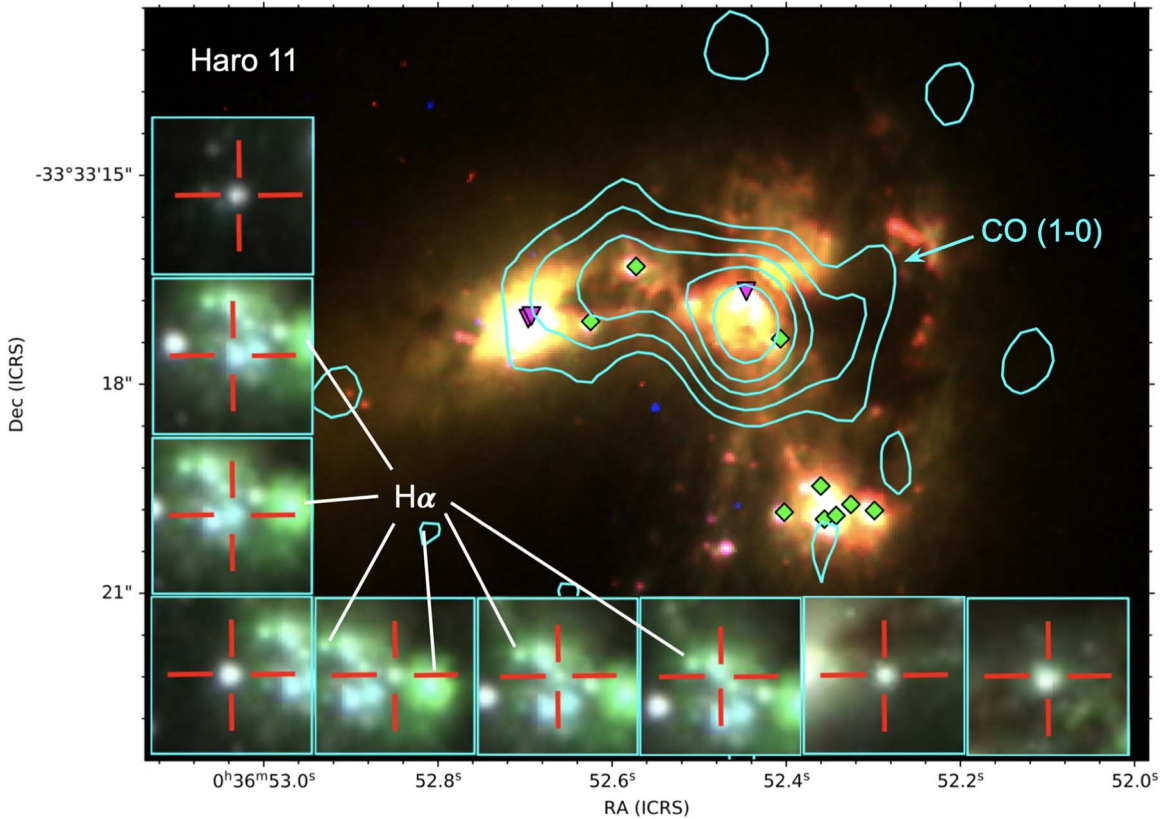


Figure 5. Contours of CO (1–0) are plotted on top of an HST NUV– B – V three-color image of Haro 11. The strongest CO emission is approximately coincident with Knot B, one of three nuclear regions (identified by purple triangles) that have been removed from the cluster sample. The second strongest peak is coincident with a bright, optical cluster. There is also weak CO emission in the dusty region to the west of these strong CO-emitting regions, and in the region to the south where the most massive young clusters have formed. The nine most massive clusters younger than ~ 15 – 20 Myr are identified by green diamonds, along with $1''.4 \times 1''.3$ postage stamps showing what they look like in the B – V – I filters. None of these nine clusters have $H\alpha$ emission (seen as green emission in the postage stamps) directly associated with them, although there are a couple of strong $H\alpha$ -emitting sources near some of these clusters.

determined by Sirressi et al. (2022) based on photometry made from the same observations used here, although no estimate of Γ was made.

There are some important differences in the results between our work and that of Adamo et al. (2011a, 2011b) for ESO 185 and Haro 11. For ESO 185, Adamo et al. (2011a) find ~ 25 clusters with $E(B - V)$ between 0.5 and 1.2 mag (see their Figure 10), despite the low dust content in this dwarf galaxy. They find 10 clusters with ages $\log(\tau/\text{yr}) < 7.0$ and masses $M > 10^5 M_\odot$, whereas we find a single cluster in this age–mass range (“1” in the left panel of Figure 6). In fact, Adamo et al. (2011a) find that a majority of clusters are younger than $\log(\tau/\text{yr}) < 7.0$, and only nine clusters in their sample have estimated ages of $\log(\tau/\text{yr}) = 8.0$ – 9.0 (see their Figure 11). Our age-dating, meanwhile, finds 130 (more than 10 times as many) clusters with ages of $\log(\tau/\text{yr}) = 8.0$ – 9.0 .

We find more subtle differences in the age-dating results for Haro 11. Adamo et al. (2011a) find ~ 15 clusters with $E(B - V) \geq 0.5$ mag, and a dominant, very young ~ 3 – 5 Myr cluster population with masses approaching $10^7 M_\odot$, and almost no clusters older than $\log(\tau/\text{yr}) = 7.6$. We also find very massive clusters younger than $\log(\tau/\text{yr}) < 7.0$, although the most massive cluster in our sample (designated as “1” in the right panel of Figure 6) is about half the mass of theirs, and we only find a handful of clusters are best fit with $E(B - V) \approx 0.5$ mag. The most notable difference is the estimated ages of the most massive clusters in the two works—here we find ages of ~ 15 – 20 Myr from our broadband plus $H\alpha$ photometry, while

Adamo et al. (2011a) find ≈ 3 – 4 Myr (but did not have $H\alpha$ photometry). Sirressi et al. (2022), meanwhile, find six clusters younger than 10 Myr with estimated masses $\approx 10^7 M_\odot$, significantly more than in Adamo et al. (2011b) or this work. We suspect this is due to their assumption of a high maximum $E(B - V)$ of 1.5 mag during age-dating, and details of their SED fitting process. As described earlier, we have visually inspected all of our ~ 15 – 20 Myr clusters and believe our age-dating is correct, since none of these clusters have $H\alpha$ emission associated with them.

We believe there are two main reasons for the differences described above: (1) we include $H\alpha$ photometry directly in the SED fits, and (2) Adamo et al. (2010, 2011a) adopted a significantly higher maximum $E(B - V)$ of 1.5 mag in their age-dating procedure, compared with the 0.1 mag we adopt for nearly all clusters. SED fits that only include broadband colors struggle to break the age–reddening degeneracy and can result in a number of systematic, ‘catastrophic’ failures in age-dating, with many older clusters with little reddening erroneously fit by a combination of young age and high reddening (e.g., Whitmore et al. 2020, 2023; M. Floyd et al., in preparation). Including $H\alpha$ photometry directly in the SED fits helps break the age–reddening degeneracy in many cases (e.g., Chandar et al. 2016; Ashworth et al. 2017). We suspect that the high maximum reddening adopted by Adamo et al. (2010, 2011b) for these low-metallicity dwarf galaxies with low dust content resulted in a number of clusters erroneously fit by a combination of too young age plus too high reddening. This

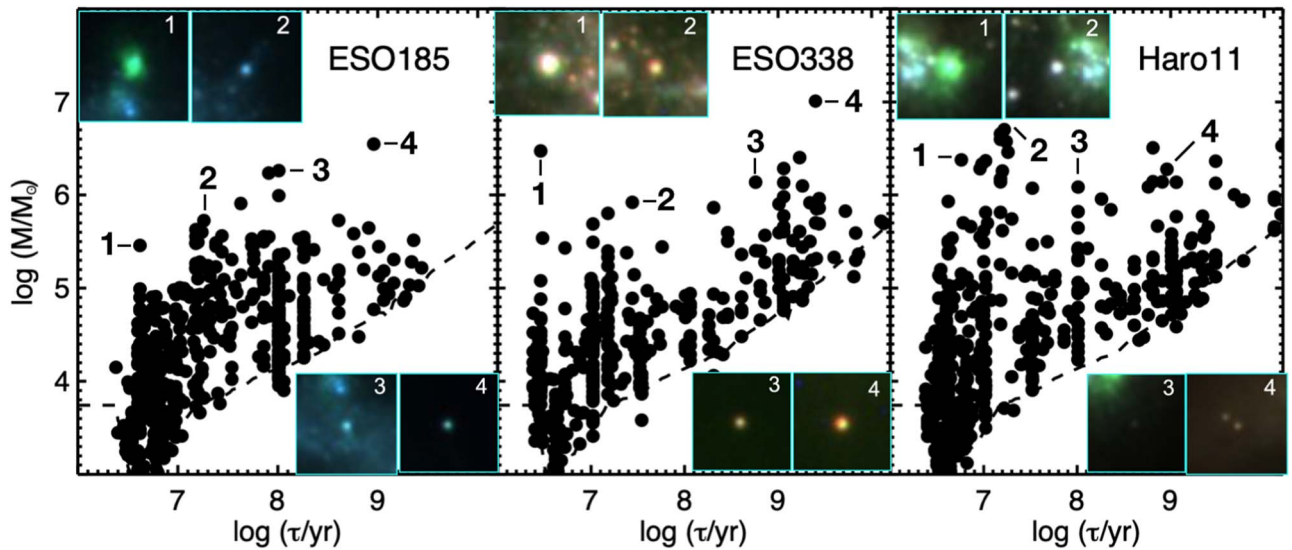


Figure 6. Cluster age–mass diagrams for our sample galaxies. The dashed line represents $M_V = -8$ mag, the approximate brightness limit for individual stars, and shows that our sample does not include older clusters at lower masses. The cluster population in each dwarf galaxy has a unique mass–age distribution. Postage stamp $B-V-I$ images of clusters of different ages are shown, as indicated. The very young 3–6 Myr clusters in ESO 185 and Haro 11 (for example, those labeled “1”) have strong $H\alpha$ emission associated with them, while the ≈ 15 –20 Myr clusters (e.g., labeled “2”) do not.

essentially moved clusters in the age–mass diagram from ages near clusters designated “2” and/or “3” in Figure 6 to ages near those designated “1.” We discuss the impact this common age-dating problem may have had on previous estimates of Γ in Section 4.4.

4. New Measurements and Implications of the Cluster Formation Efficiency

Despite nearly a decade and a half of observational work, the relationship between Γ and Σ_{SFR} (or SFR) remains unclear in nearby galaxies. Estimates of Γ in galaxies with both high and low Σ_{SFR} in particular are needed to solidify the observational picture and to compare with current simulations.

4.1. Estimates of Γ

The three BCDs studied in this work have among the highest published estimates of $\Gamma_{1-10 \text{ Myr}}$, and also among the highest Σ_{SFR} for galaxies within 100 Mpc. In Section 2 we noted a key shortcoming in the previous estimates of $\Gamma_{1-10 \text{ Myr}}$ for these galaxies, in that the estimated ages and masses for a subset of the clusters are likely incorrect, as a result of specific (common) assumptions made during SED fitting. In this section we calculate new values of Γ (in three age intervals) and compare with results published for galaxies with low Σ_{SFR} .

We follow the exact same methodology as Cook et al. (2023) and estimate $\Gamma_{1-10 \text{ Myr}}$ to be the mass of stars born in (1–10 Myr) clusters divided by the total stellar mass formed over this time period. The total mass in clusters is determined in two parts. The first is a sum of cluster masses above a given (\approx completeness) limit. We determine this completeness limit M_{lim} in each age interval to be the value where the mass function begins to fall significantly below an extrapolated power law, as shown in Figure 8 in Appendix. The second part extrapolates a power-law mass function with an index of $\beta = -2$ below the completeness limit down to an assumed minimum cluster mass of $10^2 M_\odot$. This assumed shape is consistent with the observed cluster mass functions in our BCDs, which are presented and discussed in Appendix. The

Table 3
The Fraction of Stars in Clusters

Galaxy Name	$\Gamma_{1-10 \text{ Myr}}$ This Work (%)	$\Gamma_{1-10 \text{ Myr}}$ Adamo (%)	$\Gamma_{10-100 \text{ Myr}}$ This Work (%)	$\Gamma_{100-400 \text{ Myr}}$ This Work (%)
ESO 185-IG13	15 ± 4	26 ± 5	7.4	1.5
ESO 338-IG04	39 ± 10	50 ± 10	6.5	0.8
Haro 11	18 ± 5	50_{-15}^{+13}	5	0.5

total mass in stars, i.e., the denominator, is calculated as the elapsed time \times the assumed star formation rate. We assume the SFRs compiled in column 4 of Table 1 and an uncertainty of 25%.

We assess whether incompleteness significantly impacts our results for Γ . The dominant source of incompleteness is our inability to identify faint (i.e., lower-mass) clusters in regions with high background. Incompleteness will result in artificially low estimates for Γ if we assume too low a value for M_{lim} , but Γ should be stable for values of M_{lim} that are unaffected by incompleteness. Therefore, a simple test is to estimate Γ using different values of M_{lim} . We find that the Γ estimates are nearly identical if we adopt values for M_{lim} higher than those shown in Figure 8, and drop if we adopt lower values, as expected. Therefore, incompleteness does not adversely impact our estimates of Γ . We also find that the specific apertures used for cluster photometry and to estimate the background have a negligible impact on our Γ estimates. If we adopt the age-dating results when a higher maximum $E(B-V)$ value is allowed in the fits, Γ increases to $\sim 26\%$ and $\sim 30\%$ for ESO 185-IG13 and Haro 11, respectively.

Our estimated values of $\Gamma_{1-10 \text{ Myr}}$ range from $\approx 15\%$ to 39% , and are compiled in Table 3. We find that $\Gamma_{1-10 \text{ Myr}}$ estimated from a second, independent code returns nearly identical values. We also compile the $\Gamma_{1-10 \text{ Myr}}$ results reported by Adamo et al. (2010, 2011b) for all three galaxies. These are all systematically higher than our results, with $\Gamma_{1-10 \text{ Myr}} = 50\%$ for

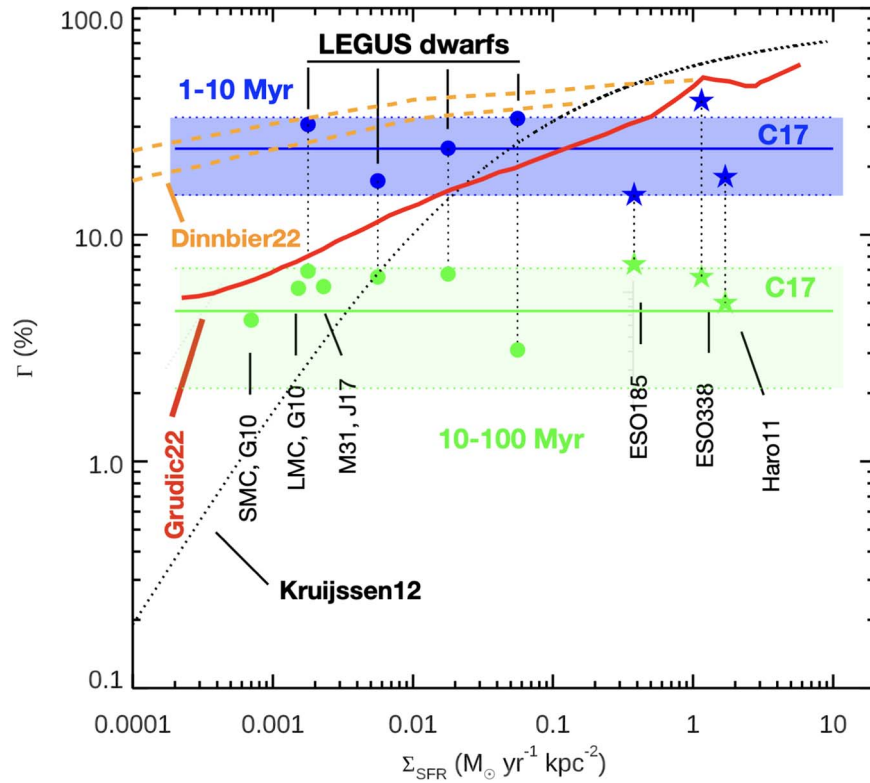


Figure 7. Our new estimates of $\Gamma_{1-10 \text{ Myr}}$ and $\Gamma_{10-100 \text{ Myr}}$ are shown by the blue and green stars, respectively. The blue and green shaded regions show the mean and standard deviation for $\Gamma_{1-10 \text{ Myr}}$ ($24\% \pm 9\%$) and $\Gamma_{10-100 \text{ Myr}}$ ($4.5\% \pm 2.5\%$) from the eight galaxies studied by Chandar et al. (2017). The filled circles show literature values for cluster formation efficiency, color-coded by age, determined for galaxies with a low Σ_{SFR} . Composite values of $\Gamma_{1-10 \text{ Myr}}$ and $\Gamma_{10-100 \text{ Myr}}$ estimated from 23 dwarf galaxies in four bins of Σ_{SFR} from the LEGUS survey (Cook et al. 2023) are included, along with estimates of $\Gamma_{10-100 \text{ Myr}}$ for M31 (Johnson et al. 2016) and the Small and Large Magellanic Clouds (Goddard et al. 2010).

ESO 338 and Haro 11 and $\Gamma \approx 26\%$ for ESO 185. We discuss the likely reasons for the discrepancies in Section 4.4.

We use the same methodology to estimate the fraction of stars found in older, surviving clusters, and compile the results in Table 3. Older clusters hold on to fewer stars, with $\Gamma_{10-100 \text{ Myr}} \approx 5\% - 8\%$ and $\Gamma_{100-400 \text{ Myr}} \approx 1\% - 2\%$. These results, however, are less certain than those for $\Gamma_{1-10 \text{ Myr}}$ because we do not have a way to directly determine the average SFR in these specific age intervals.

4.2. How Does Γ Vary with the Intensity of Star Formation?

We show one of the main results of this work in Figure 7. Our new calculations are shown as the large blue ($\Gamma_{1-10 \text{ Myr}}$) and green ($\Gamma_{10-100 \text{ Myr}}$) star symbols and plotted against Σ_{SFR} . The blue and green shaded regions show the mean and standard deviation of $\Gamma_{1-10 \text{ Myr}} = 24\% \pm 9\%$ and $\Gamma_{10-100 \text{ Myr}} = 4.5\% \pm 2.5\%$, respectively, from the eight galaxies studied by Chandar et al. (2017). Our new results for the BCD galaxies fall within their respective age ranges within the errors.

Figure 7 also plots results published for galaxies with lower Σ_{SFR} . Cook et al. (2023) recently grouped 23 nearby dwarf galaxies observed as part of the LEGUS project into four bins of Σ_{SFR} , to improve cluster statistics. We present their binned results based on SFR estimates derived from counts of young stars, stellar clusters, and associations (Cignoni et al. 2019),

and shown in Figure 7 as blue ($\Gamma_{1-10 \text{ Myr}}$) and green ($\Gamma_{10-100 \text{ Myr}}$) circles. We also include commonly cited $\Gamma_{10-100 \text{ Myr}}$ results for three other galaxies: the LMC and SMC (Goddard et al. 2010)¹² and M31 (Johnson et al. 2016).

Together, the galaxies in Figure 7 cover a range of more than 3000 in Σ_{SFR} , sufficiently large to draw conclusions about the relationship between $\Gamma_{1-10 \text{ Myr}}$ (and $\Gamma_{10-100 \text{ Myr}}$) and Σ_{SFR} . The best fit for each age interval is consistent with no correlation (slope of 0). This suggests there is no significant trend in the cluster formation efficiency $\Gamma_{1-10 \text{ Myr}}$ with Σ_{SFR} over the plotted range. $\Gamma_{10-100 \text{ Myr}}$ also shows no correlation with Σ_{SFR} .

Figure 7 also includes three separate predictions that were shown in Figure 1, which bracket the range and include the strongest correlation between Γ and Σ_{SFR} (Kruijssen 2012), a moderate one (Grudić et al. 2022), and the weakest one (Dinnbier et al. 2022). The figure demonstrates that the weakest predicted correlation by Dinnbier et al. (2022) best matches the observational results.

4.3. Does the Fraction of Stars in Clusters Evolve over Time?

Figure 8 shows a second important result. Our calculations for ESO 185, ESO 338, and Haro 11 suggest that the fraction of stars in clusters decreases from $\Gamma_{1-10 \text{ Myr}} \approx 15\% - 39\%$ (blue stars) to $\Gamma_{10-100 \text{ Myr}} \approx 5\% - 8\%$ (green stars), and decreases again for $\Gamma_{100-400 \text{ Myr}} \approx 1\% - 2\%$ (red stars). Results published previously by Chandar et al. (2017) for eight galaxies (LMC,

¹² Goddard et al. (2010) found values of $5.8\% \pm 0.5\%$ (LMC) and $4.2^{+0.2}_{-0.3}\%$ (SMC) for $\Gamma_{10-100 \text{ Myr}}$, very similar to the calculations of $5^{+3}_{-1}\%$ (LMC) and $3^{+2}_{-1}\%$ (SMC) made by Chandar et al. (2017) for the same age interval.

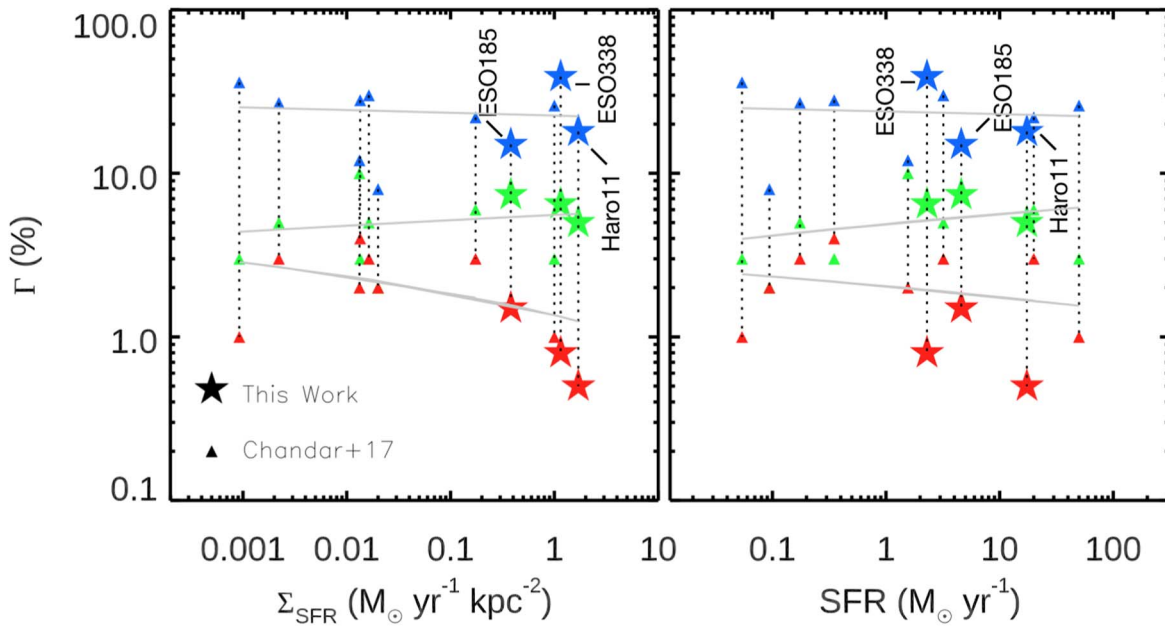


Figure 8. Estimates of $\Gamma_{1-10 \text{ Myr}}$ (blue stars), $\Gamma_{10-100 \text{ Myr}}$ (green stars), and $\Gamma_{100-400 \text{ Myr}}$ (red stars) for the BCD galaxies ESO 185-IG13, ESO 338-IG04, and Haro 11, studied here. Results from Chandar et al. (2017) for eight galaxies, including irregulars, spirals, dwarf starbursts, and ongoing mergers, are shown as the triangles. The main result of this figure is that the fraction of stars in clusters declines as the clusters age at all Σ_{SFR} .

SMC, NGC 4214, NGC 4449, M83, M51, the Antennae, and NGC 3256) show similar declines in the fraction of stars that remain in clusters over time. These are plotted as the triangles in Figure 8, and color-coded in the same way as for our BCD galaxies.

We plot the calculations for Γ in all three age intervals versus Σ_{SFR} in the left panel, and versus SFR in the right panel. The best-fit relation in each age range is shown by the gray lines in Figure 8, with no obvious difference between Σ_{SFR} and SFR. Each line is essentially flat, within the errors (i.e., has a slope consistent with 0). Our results indicate that the fraction of stars that remain in clusters decreases over time. To date, few works (besides our own) have published results for $\Gamma_{100-400 \text{ Myr}}$. In fact, this is the first work to present calculations of $\Gamma_{100-400 \text{ Myr}}$ for BCDs. It will be important for future works to include calculations in this age range to better disentangle cluster formation and disruption.

4.4. Why We Find a Different Γ - Σ_{SFR} Trend than Previous Studies

There are two primary reasons we find little to no correlation between Γ and Σ_{SFR} , while most previous observational works claim a strong correlation. The first is that previous works have plotted results from different age ranges for different galaxies, directly comparing $\Gamma_{10-100 \text{ Myr}}$ for galaxies that have low Σ_{SFR} with $\Gamma_{1-10 \text{ Myr}}$ for galaxies with high Σ_{SFR} . It is clear from Figure 7 that a plot that included the green circles representing $\Gamma_{10-100 \text{ Myr}}$ for the LMC, SMC, and M31, and also the blue stars representing $\Gamma_{1-10 \text{ Myr}}$ for ESO 185, ESO 338, and Haro 11, would roughly follow the trend of increasing Γ with Σ_{SFR} predicted by Grudić et al. (2022) and shown by the red line. This type of mixed-age comparison of observational results is biased and incorrect, yet has been presented in many works, including observation-based studies (e.g., Goddard et al. 2010; Adamo et al. 2015, 2020; Johnson et al. 2016; Messa et al. 2018) and theoretical ones (e.g., Kruijssen 2012; Li et al.

2017, 2018; Lahén et al. 2019). This bias was first pointed out by Chandar et al. (2017), and is easy to correct. For Γ , in future only results calculated from the exact same age interval should be compared between galaxies.

The second reason is more subtle yet fundamental, because it is related to correctly age-dating clusters. To estimate the age, reddening, and mass of clusters in star-forming galaxies, it is standard to perform some type of SED fitting, where measured broadband colors are compared with predictions from stellar evolutionary models (similar to the method described in Section 3.1). The main challenge is to break the age–reddening degeneracy, since clusters can appear red because they are older or because they are reddened due to the presence of dust (e.g., Adamo et al. 2010; Calzetti et al. 2015; Turner et al. 2021). Usually there are two or three combinations of age and reddening that match the measured broadband colors of a cluster (e.g., see Figure 4 in Whitmore et al. 2023). Including information on whether or not line emission is present, from $\text{H}\alpha$ photometry for example, significantly improves age estimates by distinguishing between very young, $\text{H}\alpha$ -emitting clusters and older ones that no longer show line emission (e.g., Chandar et al. 2010b; Fouesneau et al. 2012; Ashworth et al. 2017; Whitmore et al. 2020).

A high maximum allowed $E(B - V)$ in age-dating can lead to catastrophic age and mass determinations for some clusters when no narrowband photometry is included (as described in detail by Whitmore et al. 2020, 2023). During the fitting procedure, the same range of reddening (from 0.0 up to some maximum $E(B - V)$) is typically adopted for all clusters, regardless of how much dust is nearby. As discussed in Section 3.2, we believe that a number of older clusters in ESO 185, ESO 338, and Haro 11 were fit with ages younger than $\log(\tau/\text{yr}) \lesssim 7.0$ by Adamo et al. (2010, 2011a) because they adopted a high maximum value of $E(B - V) = 1.5 \text{ mag}$ ($A_V \sim 4.8 \text{ mag}$ for a Milky Way–like extinction curve) for all clusters but did not have $\text{H}\alpha$ photometry to help break the age–reddening degeneracy.

We perform several experiments to assess the impact that catastrophic age-dating could have on $\Gamma_{1-10 \text{ Myr}}$. For ESO 185, Adamo et al. (2010) found 10 very young $<10 \text{ Myr}$ clusters with masses $\geq 10^5 M_\odot$, while we found a single cluster that satisfies this age–mass criterion. We find that our result for $\Gamma_{1-10 \text{ Myr}}$ nearly doubles and is similar to that found by Adamo et al. (2011b) if we artificially match the number (10) and approximate masses of their clusters in this age–mass regime. For Haro 11, if we approximately double the mass of the most massive $<10 \text{ Myr}$ cluster to match that in Adamo et al. (2011b), $\Gamma_{1-10 \text{ Myr}}$ increases by $\sim 10\%$. If we assume the most (three most, five most) massive clusters with ages $\sim 15\text{--}20 \text{ Myr}$ were age-dated to $\sim 3\text{--}6 \text{ Myr}$, we find $\Gamma_{1-10 \text{ Myr}}$ increases by $\sim 6\%$ ($\sim 15\%$, $\sim 24\%$). These differences can account for the offset between our results and Adamo et al.’s for $\Gamma_{1-10 \text{ Myr}}$. Our experiments establish that the systematic age-dating error that affected previous studies of the cluster populations in ESO 185 and Haro 11 (and likely ESO 338) quite likely led to an artificial increase in $\Gamma_{1-10 \text{ Myr}}$.

5. Summary and Conclusions

Nearly all current simulations of cluster formation and early evolution predict that the fraction of stars that form in bound clusters increases with the amount of star formation per area or Σ_{SFR} in the host galaxy, although the exact relationship varies significantly between different works. However, these simulations rely on a large number of uncertain inputs and prescriptions, particularly for star formation and stellar feedback. Because BCD galaxies have among the highest measured Σ_{SFR} within 100 Mpc, their cluster populations provide important input and constraints on simulations.

The fraction of stars formed in 1–10 Myr clusters, or $\Gamma_{1-10 \text{ Myr}}$, was previously estimated to be $\sim 50\%$ for the BCD galaxies ESO 338 and Haro 11, and $\sim 26\%$ for ESO 185 (Adamo et al. 2010, 2011a). In this work, we found significantly lower values of $15\% \pm 4\%$ (ESO 185), $39\% \pm 10\%$ (ESO 338), and $18\% \pm 5\%$ (Haro 11), based on deeper HST observations that include narrowband $H\alpha$ imaging taken as part of the CCDG survey. We compared our new results with previous ones for galaxies with lower Σ_{SFR} , and found that $\Gamma_{1-10 \text{ Myr}}$ does *not* vary with Σ_{SFR} , over a range of ≈ 3000 in Σ_{SFR} , whereas current simulations predict an increase by a factor between ~ 1.5 and 100 over our observed range of Σ_{SFR} . We also found the fraction of stars that remain in older clusters drops to $\Gamma_{10-100 \text{ Myr}} \approx 5\%\text{--}8\%$, and to $\Gamma_{100-400 \text{ Myr}} \approx 1\%\text{--}2\%$ in our BCDs, as expected due to early cluster disruption.

We believe there are two reasons why our results contradict previous works that have claimed a strong dependence of cluster formation efficiency on Σ_{SFR} . The first is that the previously reported increase was based on mixing results for $\Gamma_{1-10 \text{ Myr}}$ for galaxies with higher Σ_{SFR} with $\Gamma_{10-100 \text{ Myr}}$ for galaxies with lower Σ_{SFR} . Specifically, $\Gamma_{10-100 \text{ Myr}}$ values determined for the SMC and LMC by Goddard et al. (2010) and for M31 by Johnson et al. (2017) have regularly been compared with $\Gamma_{1-10 \text{ Myr}}$ estimates for galaxies such as ESO 185, ESO 338, and Haro 11. It is critical that future comparisons of Γ between galaxies are based on the exact same age intervals.

The second reason for the discrepancy is a key new finding of this work. Previous age estimates for a number of older clusters in the BCD galaxies studied here appear to have been

erroneously underestimated and best fit with very young $<10 \text{ Myr}$ ages and moderate reddening. This age-dating error artificially boosted the estimates of mass and $\Gamma_{1-10 \text{ Myr}}$. We believe the age-dating concerns identified in this work may have affected a number of previous studies as well.

If confirmed, the observational results from this work present a challenge to most current theoretical models and simulations of cluster formation, because they suggest that, at least on galactic scales, outcomes of the star and cluster formation process do not vary strongly with the intensity of star formation.

R.C. acknowledges support from HST-GO-15469. We thank the anonymous referee for suggestions that improved our paper.

This work is based on observations made with the NASA/ESA Hubble Space Telescope, obtained from the data archive at the Space Telescope Science Institute. STScI is operated by the Association of Universities for Research in Astronomy, Inc. under NASA contract NAS 5-26555.

Appendix

Cluster Mass Functions in Blue Compact Dwarfs

A number of cosmological simulations that form entire cluster populations have measured the initial cluster mass function that is produced. Some of these simulations find an initial cluster mass function that is better represented by a Schechter function than by a power law, with an upper mass cutoff M_* that increases with Σ_{SFR} (e.g., Li et al. 2018; Pfeffer et al. 2019). A Schechter-like shape suggests there is a physical upper mass with which clusters can form out of the interstellar medium. Other simulations, for example from FIRE-2 (Grudić et al. 2022), create more complicated mass functions, which vary over time and by region and do not follow a simple power law and/or Schechter distribution.

The observed shape of the cluster mass function in different galaxy environments, particularly whether or not there is a physical cutoff or truncation at the upper end, provides important constraints on the relationship between clusters and molecular clouds. In this Appendix, we present the first assessment of the shapes of the cluster mass functions in ESO 185-IG13, ESO 338-IG04, and Haro 11, and find that they are well represented by a single power law, $dN/dM \propto M^\beta$, with $\beta \approx -2$.

A.1. Maximum Likelihood Fits

In Figure 9, we present the cumulative cluster mass functions in three age intervals: 1–10 Myr (left), 10–100 Myr (middle), and 100–400 Myr (right), with results for ESO 185 shown in the top panels, ESO 338 in the middle, and Haro 11 in the bottom panels. We determine the completeness limit as the mass at which each distribution begins to fall significantly below an extrapolated power law (by a factor of ~ 2 ; see Mok et al. 2019, 2021). These lower mass limits are shown as dashed vertical lines, and adopted for the maximum likelihood fits described below as well as the Γ calculations presented in Section 4.1. The best-fit power law and truncated power law from the MSPECFIT code (Rosolowsky 2005) are shown in each panel, as indicated. The indices β of the best-fit power law $dN/dM \propto M^\beta$ are all between -1.6 and -2.1 , with a median of $\beta = -1.9$.

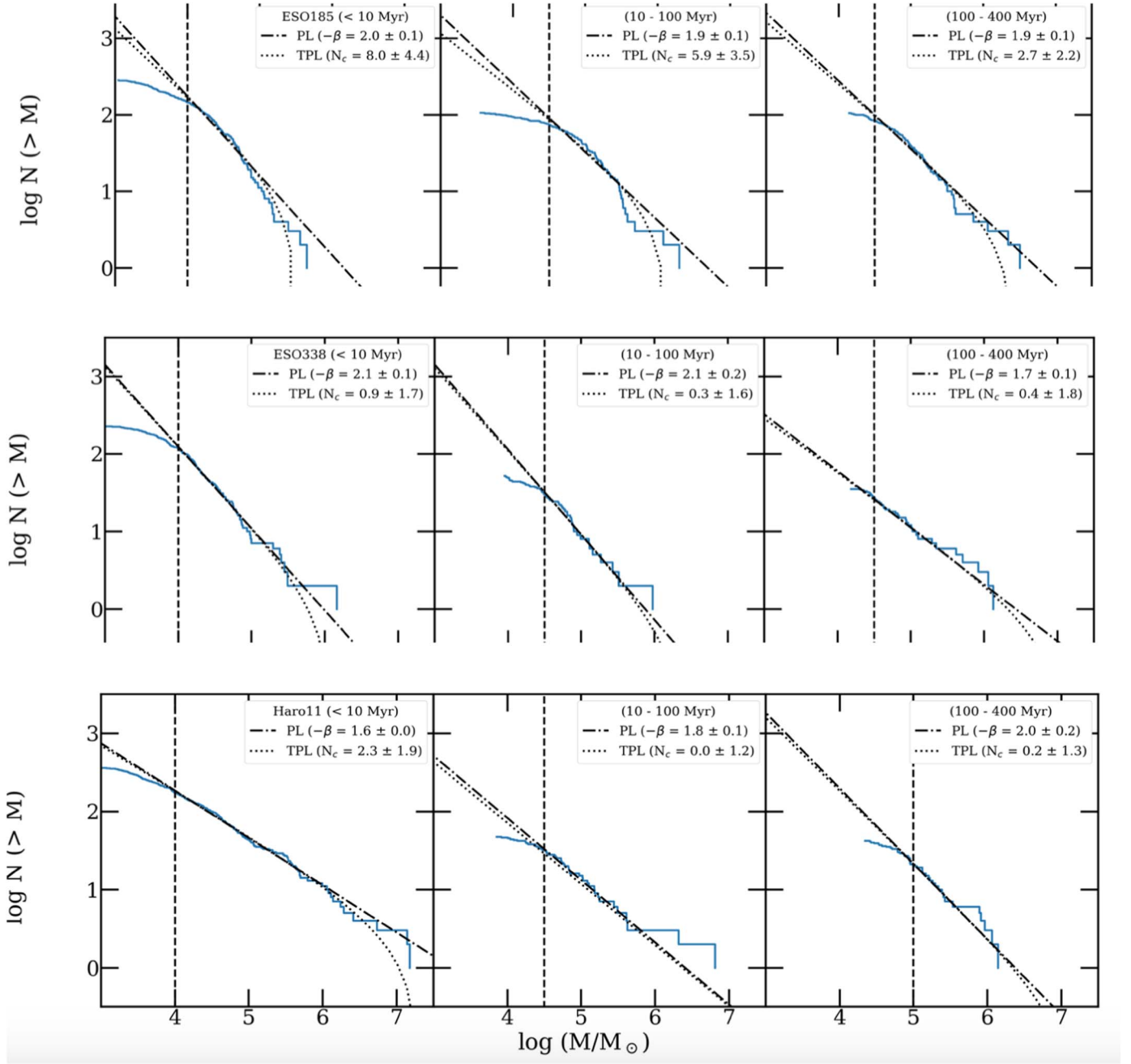


Figure 9. Cumulative mass functions are shown in blue for the indicated age intervals. The best-fit power law is shown as the dashed–dotted line and the best-fit Schechter function as the dotted line. The best-fit power-law index β and the statistic related to whether or not there is a truncation in the power law are listed in each panel. The vertical dashed lines show the lower mass value used in the maximum likelihood analysis.

We use the maximum likelihood method described in Mok et al. (2019) to determine the best-fit value and confidence intervals for β and M_* when fitting a Schechter function to the cluster masses above the completeness limit, $\psi(M) \propto M^\beta \exp(-M/M_*)$. This method does not use binned data, which can hide weak features at the ends of the distribution, or cumulative distributions, where the data points are not independent of one another. We compute the likelihood $L(\beta, M_*) = \prod_i P_i$ as a function of β and M_* , where the probability P_i for each cluster is given by

$$P_i = \frac{\psi(M_i)}{\int_{M_{\min}}^{\infty} \psi(M) dM} \quad (\text{A1})$$

and the product is over all clusters above the completeness limit (see, e.g., Chapter 15.2 of Mo et al. 2010). We set the upper integration limit in Equation (A1) to be 100 times the mass of the most massive cluster, which is sufficient for convergence. Next, we find the maximum likelihood L_{\max} using the Nelder & Mead (1965) method, and use the standard formula

$$\ln L(\beta, M_*) = \ln L_{\max} - \frac{1}{2} \chi_p^2(k) \quad (\text{A2})$$

where $\chi_p^2(k)$ is the chi-squared distribution with k degrees of freedom at confidence level p to determine the 1σ , 2σ , and 3σ confidence contours.

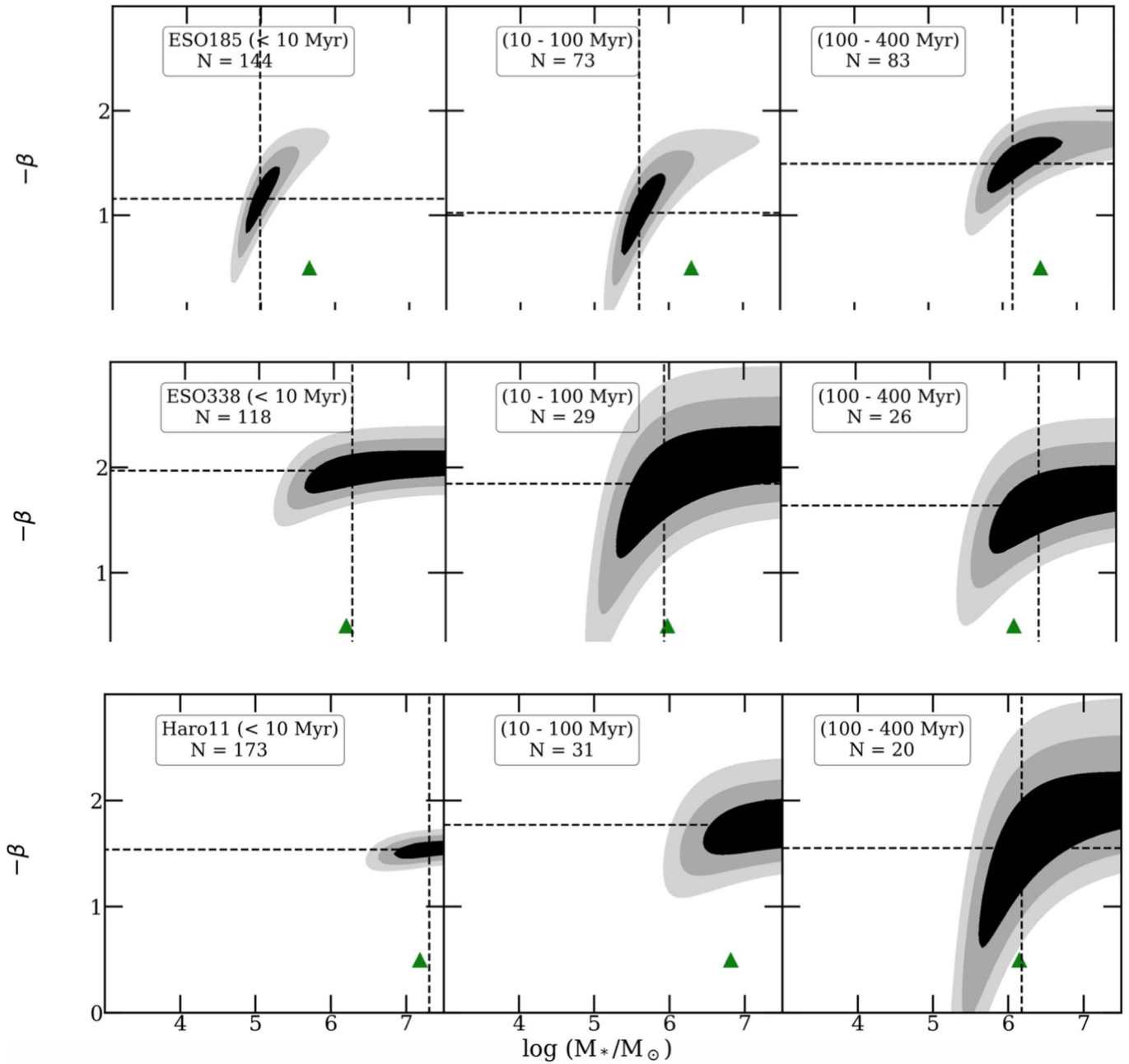


Figure 10. Likelihood fits of the Schechter parameters β and M_* to cluster masses in three age intervals, <10 Myr (left), 10–100 Myr (center), and 100–400 Myr (right). Results for ESO 185 are in the top panels, ESO 338 in the middle, and Haro 11 in the bottom panels. The dashed lines show the best-fit values of β and M_* , while the boundaries of the shaded regions show the 1 σ , 2 σ , and 3 σ confidence contours. The green triangles show the maximum cluster mass in each sample.

Figure 10 shows the best-fit values of β and M_* (dashed lines) that result from our maximum likelihood fitting analysis. The shaded regions show the 1 σ , 2 σ , and 3 σ contours. The contours show a short diagonal portion, which indicates the trade-off between a steeper value of β and a higher cutoff mass M_* , and then a relatively flat portion up to the highest mass tested. The green triangle shows the most massive cluster in each sample. We do not include uncertainties in the cluster mass estimates in the fits, which would serve to further increase the uncertainties in the Schechter parameters β and M_* .

A.2. Implications for the Upper End of the Cluster Mass Function

We are interested in answering the question: is there a physical mass limit with which clusters can form in ESO 185, ESO 338, and Haro 11, and if so, can we detect it? As in our previous studies, we performed fits to the mass function of clusters in the 1–10 Myr, 10–100 Myr, and 100–400 Myr age intervals. Ideally, we should find consistent estimates of, or limits on, the Schechter parameters β and M_* in all three intervals, since the physics of cluster formation are unlikely to change significantly over the relatively short period of 4×10^8 yr covered by our study. It is physically implausible for the upper cutoff M_* to increase with age, but quite possible

that systematic errors could affect the fit results. The 100–400 Myr interval covers the longest elapsed time, so for a given SFR, this interval is likely to be the most reliable for determining β and M_* (Mok et al. 2019). Haro 11 is an exception, since the most massive clusters (and likely most intense star formation) occurred ≈ 15 –30 Myr ago in this galaxy, with very few clusters with ages between 100 and 400 Myr detected.

None of the fits show evidence for a specific upper mass cutoff in ESO 338 and Haro 11, since the horizontal confidence contours continue without closing to the right edge of the diagrams. This means that the cluster masses are consistent with being drawn from a single power law, but an upper cutoff (over this range of M_*) cannot be ruled out. These results indicate that the value of M_* returned by the maximum likelihood fit is indeterminate and represents a lower limit to the actual value. For ESO 185, the two younger age intervals show weak evidence for a cutoff M_* with a very shallow estimate of $\beta \approx -1$; this shallow value of β reflects correlations between the exponent β and cutoff M_* , since there is a trade-off between a steeper value of β and a higher value of M_* . Taken at face value, the best-fit value of M_* increases with age, which is unlikely to be a physical result. We conclude that the three BCD galaxies studied here have cluster masses that are consistent with being drawn from a pure power law, with a wide range of permitted cutoff masses from $M_* \approx 10^6 M_\odot$ to ∞ .

ORCID iDs

Rupali Chandar  <https://orcid.org/0000-0003-0085-4623>
 Miranda Caputo  <https://orcid.org/0000-0002-2957-3924>
 Angus Mok  <https://orcid.org/0000-0001-7413-7534>
 Sean Linden  <https://orcid.org/0000-0002-1000-6081>
 Bradley C. Whitmore  <https://orcid.org/0000-0002-3784-7032>
 David O. Cook  <https://orcid.org/0000-0002-6877-7655>
 Janice C. Lee  <https://orcid.org/0000-0002-2278-9407>
 Richard White  <https://orcid.org/0000-0002-9194-2807>

References

- Adamo, A., Kruijssen, J. M. D., Bastian, N., Silva-Villa, E., & Ryon, J. 2015, *MNRAS*, 452, 246
 Adamo, A., Hollyhead, K., Messa, M., et al. 2020, *MNRAS*, 499, 3267
 Adamo, A., Östlin, G., Zackrisson, E., et al. 2010, *MNRAS*, 407, 870
 Adamo, A., Östlin, G., Zackrisson, E., & Hayes, M. 2011a, *MNRAS*, 414, 1793
 Adamo, A., Östlin, G., & Zackrisson, E. 2011b, *MNRAS*, 417, 1904
 Ashworth, G., Fumagalli, M., Krumholz, M. R., et al. 2017, *MNRAS*, 469, 2464
 Bruzual, G., & Charlot, S. 2003, *MNRAS*, 344, 1000
 Calzetti, D., Lee, J. C., Sabbi, E., et al. 2015, *AJ*, 149, 51
 Chabrier, G. 2003, *PASP*, 115, 763
 Chandar, R., Fall, S. M., & Whitmore, B. C. 2010a, *ApJ*, 711, 1263
 Chandar, R., Whitmore, B. C., Kim, H., et al. 2010b, *ApJ*, 719, 966
 Chandar, R., Fall, S. M., Whitmore, B. C., & Mulia, A. J. 2017, *ApJ*, 849, 128
 Chandar, R., Whitmore, B. C., Dinino, D., et al. 2016, *ApJ*, 824, 71
 Cignoni, M., Sacchi, E., Tosi, M., et al. 2019, *ApJ*, 887, 112
 Cook, D. O., Lee, J. C., Adamo, A., et al. 2019, *MNRAS*, 484, 4897
 Cook, D. O., Lee, J. C., Adamo, A., et al. 2023, *MNRAS*, 519, 3749
 Cook, D. O., Seth, A. C., Dale, D. A., et al. 2012, *ApJ*, 751, 100
 Dinnbier, F., Kroupa, P., & Anderson, R. I. 2022, *A&A*, 660, A61
 Fall, S. M., & Chandar, R. 2012, *ApJ*, 752, 96
 Fall, S. M., Chandar, R., & Whitmore, B. C. 2005, *ApJL*, 631, L133
 Fitzpatrick, E. L. 1999, *PASP*, 111, 63
 Fouesneau, M., Lançon, A., Chandar, R., & Whitmore, B. C. 2012, *ApJ*, 750, 60
 Gaia Collaboration, Mignard, F., Klioner, S. A., et al. 2018, *A&A*, 616, A14
 Ginsburg, A., & Kruijssen, J. M. D. 2018, *ApJL*, 864, L17
 Goddard, Q. E., Bastian, N., & Kennicutt, R. C. 2010, *MNRAS*, 405, 857
 Grudić, M. Y., Hafen, Z., Rodriguez, C. L., et al. 2022, *MNRAS*, 519, 1366
 Grudić, M. Y., Hopkins, P. F., Faucher-Giguère, C.-A., et al. 2018, *MNRAS*, 475, 3511
 Hayes, M., Östlin, G., Atek, H., et al. 2007, *MNRAS*, 382, 1465
 Johnson, L. C., Seth, A. C., Dalcanton, J. J., et al. 2016, *ApJ*, 827, 33
 Johnson, L. C., Seth, A. C., Dalcanton, J. J., et al. 2017, *ApJ*, 839, 78
 Kennicutt, R. C., & Evans, N. J. 2012, *ARA&A*, 50, 531
 Kennicutt, R. C., Jr. 1998, *ApJ*, 498, 541
 Kruijssen, J. M. D. 2012, *MNRAS*, 426, 3008
 Lada, C. J., & Lada, E. A. 2003, *ARA&A*, 41, 57
 Lahén, N., Naab, T., Johansson, P. H., et al. 2019, *ApJL*, 879, L18
 Lee, J. C., Whitmore, B. C., Thilker, D. A., et al. 2022, *ApJS*, 258, 10
 Li, H., Gnedin, O. Y., Gnedin, N. Y., et al. 2017, *ApJ*, 834, 69
 Li, H., Gnedin, O. Y., & Gnedin, N. Y. 2018, *ApJ*, 861, 107
 Mas-Hesse, J. M., & Kunth, D. 1999, *A&A*, 349, 765
 McKee, C. F., & Ostriker, E. C. 2007, *ARA&A*, 45, 565
 Messa, M., Adamo, A., Östlin, G., et al. 2018, *MNRAS*, 473, 996
 Mo, H., van den Bosch, F. C., & White, S. 2010, *Galaxy Formation and Evolution* (Cambridge: Cambridge Univ. Press)
 Mok, A., Chandar, R., & Fall, S. M. 2019, *ApJ*, 872, 93
 Mok, Angus, Chandar, Rupali, & Fall, S. Michael 2021, *ApJ*, 911, 8
 Nelder, J. A., & Mead, R. 1965, *CompJ*, 7, 308
 Pfeffer, J., Bastian, N., Kruijssen, J. M. D., et al. 2019, *MNRAS*, 490, 1714
 Rosolowsky, E. 2005, *PASP*, 117, 1403
 Sirressi, M., Adamo, A., Hayes, M., et al. 2022, *MNRAS*, 510, 4819
 Turner, J. A., Dale, D. A., Lee, J. C., et al. 2021, *MNRAS*, 502, 1366
 Whitmore, B. C., Chandar, R., Lee, J., et al. 2020, *ApJ*, 889, 154
 Whitmore, B. C., Chandar, R., Lee, J. C., et al. 2023, *MNRAS*, 520, 63
 Whitmore, B. C., Chandar, R., Schweizer, F., et al. 2010, *AJ*, 140, 75